*Journal of Engineering Mathematics* **47:** 201–216, 2003.


# Intra- and interventricular asynchrony of electromechanics in the ventricularly paced heart

R.C.P. KERCKHOFFS[1], P.H.M. BOVENDEERD[1], F.W. PRINZEN[2], K. SMITS[3] and T. ARTS[1,4]

[1]*Eindhoven University of Technology, Department of Biomedical Engineering, P.O.Box 513, 5600 MB Eindhoven, The Netherlands (p.h.m.bovendeerd@tue.nl);* [2]*Maastricht University, Department of Physiology, P.O.Box 616, 6200 MD Maastricht, The Netherlands;* [3]*Medtronic Bakken Research Center, Department of lead modeling, 6229 GW Maastricht, The Netherlands;* [4]*Maastricht University, Department of Biophysics, P.O.Box 616, 6200 MD Maastricht, The Netherlands*

Received 22 May 2003; accepted in revised form 15 August 2003

**Abstract.** The degree of restoration of pump function by ventricular pacing depends on the pacing site and timing of pacing. Numerical models of cardiac electromechanics could be used to investigate the relation between the ventricular pacing site and timing on the one side, and pump function on the other. In patient-specific models, these numerical models could be used to optimize location and timing for best pump function. The aim of this study was to demonstrate the potential for modeling patient-specific electromechanic during ventricular pacing by means of the extension of an existing three-dimensional finite-element model of LV electromechanics with the right ventricle. A parametrized geometry of the LV and RV was made from canine (non-invasively obtained) cine-MR short axis images. Depolarization was modeled using the eikonal-diffusion equation. Mechanics was computed from balance of momentum, with nonlinear anisotropic passive and time-, strain-, and strainrate-dependent uniaxial active behavior. Simulations of complete cardiac cycles were performed for a normal heart beat with synchronous activation and ventricular pacing at the right ventricular apex and left ventricular free wall. We focused on timing of LV and RV hemodynamics, asynchrony in depolarization and myofiber shortening, regional stroke work, and systolic septal motion. In the simulation of sinus rhytm, ventricular ejection was found to start earlier for the right side than for the left side, which is in agreement with experimental data. In simulations with ventricular pacing, results agreed with experimental findings in the following aspects: 1) depolarization sequence; 2) the spatial distributions of sarcomere length and stroke work density depended mainly on timing of depolarization; 3) maximum pressure and maximum increase of pressure were lower than during sinus rhythm; 4) the earliest activated ventricle had the earliest start of ejection, and 5) the septum moved towards the last activated ventricle at the onset of systole. As a first step, the potential of patient-specific modeling in simulating conduction disturbances has been demonstrated by inserting a ventricular geometry, obtained from non-invasively measured short axis MR images. Later steps would include the implementation of adaptation models to estimate patient myofiber orientation and to assess the effects of pacing in the long term.

**Key words:** cardiac electromechanics, cardiac geometry, left ventricle, right ventricle, 3-D finite-element model, ventricular pacing

## 1. Introduction

The heart consists of two pumps, located side-by-side (Figure 1). The right ventricle (RV) pumps the blood to the lungs and the left ventricle (LV) to the rest of the body. Depolarization is normally initiated by self-depolarization of the sinoatrial (SA) node located at the transition between the right atrium and superior vena cava.

Next, the depolarization wave propagates over the atria through the atrioventricular (AV) node to the His bundle. The His bundle splits in a right and left branch, depolarizing the right

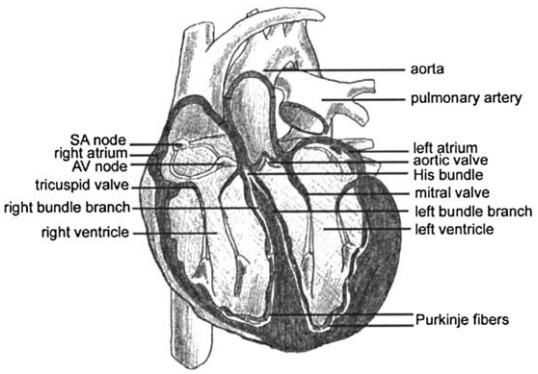


*Figure 1.* Cross-section of the heart, showing atria and ventricles, and the specialized conduction system. A part of the pulmonary artery is cut away. SA node: sino-atrial node, AV node: atrio-ventricular node. Adapted from [45, p. 395].

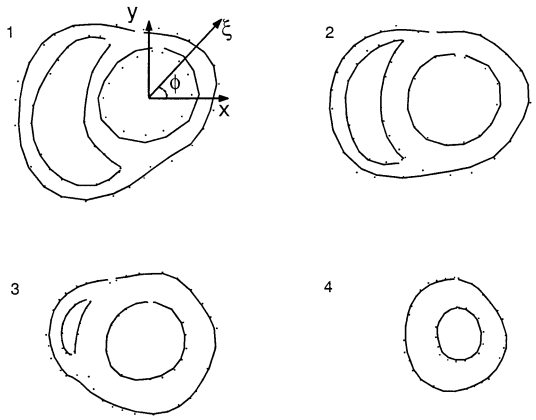


*Figure 2.* Fitted contours (lines) for four cross-sections from base (1) to near the apex (4). The dots represent the original data, as obtained manually from the MRI short axis images. The heart bound Cartesian coordinates $x$ and $y$ are shown, as well as the circumferential angle $\phi$ and radial coordinate $\xi$ from the ellipsoidal coordinate system.

and left ventricle, respectively, via networks of fast-conducting Purkinje fibers. The whole ventricular myocardium is depolarized within 40–50 ms [1]. The RV is activated somewhat earlier than the LV [2, 3]. Stress develops in all myofibers and leads to an increase of ventricular pressures. Myofiber shortening leads to ejection and equal amounts of blood are ejected by the LV and RV cavities. During ejection, systolic pressure is about 4 times higher in the LV than in the RV. Normally, contraction is approximately homogeneous and coherent.

The normal contraction pattern of the heart may be affected by abnormal conduction of the depolarization wave [4, 5], for instance when the left bundle branch is blocked [6], or during ventricular pacing. In a ventricularly paced heart, depolarization is not as synchronous as in a normal heart and stroke-work density is distributed non-uniformly [7]. The resulting more pronounced asynchrony of contraction of the myofibers affects pump function [8], myocardial tissue structure [9], and may even contribute to the development of heart failure [10, 11]. In the early years of clinical pacing, most attention was paid to proper thresholds and synchronization between atria and ventricles [12]. Recently, interest in a proper sequence and synchrony of ventricular depolarization is growing. The sequence of depolarization depends on the choice of the pacing site and on timing of pacing. Optimizing this choice is often a matter of trial and error.

An interesting challenge is to develop mathematical models incorporating patient-specific characteristics with the goal to optimize timing and location of ventricular pacing for a better pump function. Models of cardiac mechanics have been used to investigate the effect of myofiber orientation [13–15] and regional ischemia [16–18] on the distribution of myofiber stress and strain. Such models have also been used to investigate the relation between timing of depolarization and contraction [19, 20] for a normal heart beat, but not yet for ventricular pacing.

The aim of this study was to demonstrate the potential for modeling patient-specific electromechanics during ventricular pacing by means of extension of an existing three-dimensional finite-element model of LV electromechanics [19] with the right ventricle. The geometry of the LV and RV was obtained from non-invasively acquired MR short axis images of the canine heart. The myofiber helix angle [21] was assumed to vary linearly across the wall. Values of parameters describing depolarization wave propagation and mechanical properties were as presented before [19, 22]. Complete cardiac cycles were simulated for a normal heart with synchronous activation and ventricular pacing. Pacing was initiated from the endocardial right ventricular apex (RVA) of from the epicardial left ventricular free wall (LVFW). We focused on timing of LV and RV hemodynamics, asynchrony of depolarization, myofiber shortening, stroke work, and systolic septal wall motion.

## 2. Material and methods

### 2.1. Geometry and myofiber orientation

LV and RV geometries were derived from five Magnetic Resonance (MR) short axis images ($1{\cdot}17 \times 1{\cdot}17 \times 8{\cdot}0$ mm$^3$ voxel volume) in end-diastolic state of an anesthetized dog. Interpolation was performed between the images in the long axis ($z$)-direction with custom software, obtaining the contours of the heart in 20 short axis sections. The contours of the RV endocardium were subdivided in a RV free-wall partition and a RV septum partition. Thus, four sets of datapoints were obtained for the epicardial (20 contours), LV endocardial (18 contours) and RV free wall and septal (each 13 contours) surfaces (Figure 2).

From the contours, the position $\vec{r}$ of each data point was obtained in Cartesian MR coordinates $\{x_{MR}, y_{MR}, z_{MR}\}$. First, these coordinates were tranformed by rigid rotations and translations to coordinates $\{x, y, z\}$ with respect to a heartbound Cartesian system, with the origin at the intersection of the LV long axis and the most basal slice. The $z$-axis was aligned with the long axis of the LV, and the $x$-axis from RV free wall to LV free wall. To enable an efficient mathematical description of the cardiac surfaces, the latter Cartesian coordinates were transformed to prolate spheroidal coordinates $\{\xi, \theta, \phi\}$:

$$\begin{aligned} x &= C \sinh(\xi) \sin(\theta) \cos(\phi), \\ y &= C \sinh(\xi) \sin(\theta) \cos(\phi), \\ z &= C \sinh(\xi) \cos(\theta), \end{aligned} \tag{1}$$

where $C$ is the focal length of the system, $\xi$ the radial coordinate, $\phi$ the circumferential angle, and $\theta$ the longitudinal angle. All four surfaces were described by a prolate spheroidal harmonic series [23, 24]:

$$\xi(\theta, \phi) = \sum_{l=0}^{L} \sum_{m=-l}^{m=1} a_{lm} P_l^m(\cos\theta) \mathrm{e}^{\mathrm{i}m\phi}. \tag{2}$$

Here $P_l^m$ are associated Legendre polynomials, and $a_{lm}$ are coefficients, resulting from a least-squares fit (with highest order $L$) to the experimental datasets.

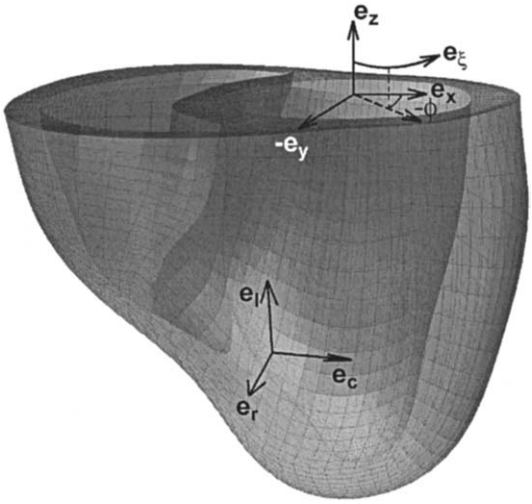


*Figure 3.* The mesh of the left and right ventricle, showing epicardium and RV and LV endocardium. The heart bound Cartesian coordinate system with orthonormal vectors $\vec{e}_x$, $\vec{e}_y$, $\vec{e}_z$ is shown. The radial direction $\vec{e}_\xi$ for a constant $\theta$ is shown at circumferential angle $\phi$. The local wall-bound coordinate system for an epicardial node is shown with $\vec{e}_r$ the radial direction, $\vec{e}_c$ circumferential direction, and $\vec{e}_l$ longitudinal direction.

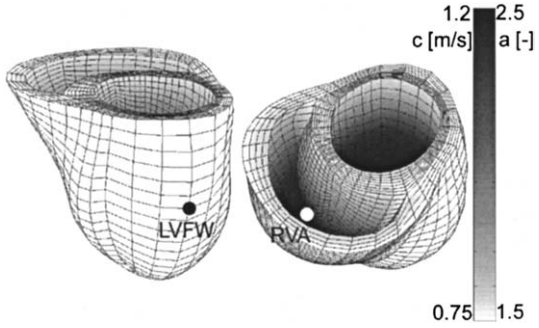


*Figure 4.* Distribution of depolarization wave velocity *c* and of anisotropy ratio *a*. The locations for pacing at the left ventricular free wall, and right ventricular apex are denoted by LVFW, and RVA, respectively.

Using the fit, for each arbitrary point on each arbitrary surface, an orthonormal wall bound pheroidal coordinate system $\{\vec{e}_r, \vec{e}_c, \vec{e}_l\}$ was defined (Figure 3):

$$\vec{e}_r = \frac{\dfrac{\partial \vec{r}}{\partial \xi}}{\left\| \dfrac{\partial \vec{r}}{\partial \xi} \right\|}, \quad \frac{\dfrac{\partial \vec{r}}{\partial \phi}}{\left\| \dfrac{\partial \vec{r}}{\partial \phi} \right\|}, \quad \frac{\dfrac{\partial \vec{r}}{\partial \theta}}{\left\| \dfrac{\partial \vec{r}}{\partial \theta} \right\|}. \tag{3}$$

Here the base vectors $\vec{e}_r$, $\vec{e}_c$ and $\vec{e}_l$ point in the local radial (transmural), circumferential and longitudinal direction, respectively. For points within the cardiac wall, the local coordinate system was obtained by interpolation of the coordinate systems at the nearest points on the inner and outer surfaces. The coordinate system was used to define the orientation of the myofibers in the wall. Myofibers were assumed to be in planes spanned by the local circumferential and longitudinal direction. The in-plane myofiber orientation was characterised by the helix angle, defined as the angle between the myofiber direction and the local circumferential direction [21]. The helix angle was assumed to vary linearly from $-70°$ at the epicardium and $70°$ at both the RV and LV endocardium. Similarly, in the septum the helix angle ranged from $-70°$ at the RV side to $70°$ at the LV side.

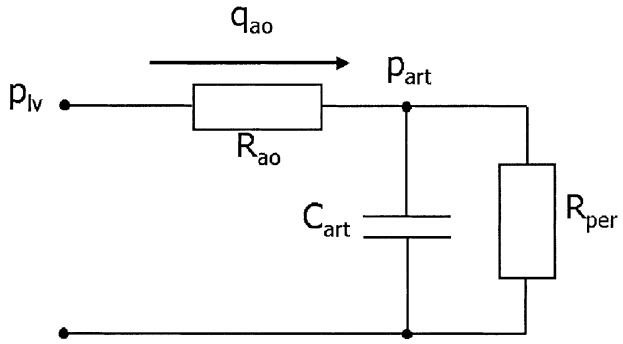


*Figure 5* Electric representation of the three-element Windkessel model used [31] for the LV. $p_{lv}$ left ventricular pressure [Pa]; $p_{art}$ arterial pressure [Pa]; $q_{a0}$ aortic flow [$m^3$/s]; $Z_{ao}$ aortic impedance [$Pa\cdot/m^3$]; $R_{per}$ peripheral resistance [$Pa\cdot s/m^3$]; $C_{art}$ arterial compliance [$m^3$/Pa].

## 2.2. Depolarization wave

For RVA and LVFW pacing (Figure 4) the moment of depolarization $t_{dep}$ was determined from solving the eikonal-diffusion equation [25] for the gradient of $t_{dep}$ ($\vec{\nabla} t_{dep}$):

$$c\sqrt{\vec{\nabla} t_{dep} \cdot \boldsymbol{M} \cdot \vec{\nabla} t_{dep}} - k\vec{\nabla} \cdot (\boldsymbol{M} \cdot \vec{\nabla} t_{dep}) = 1. \tag{4}$$

The parameter $c$ represents the velocity of the depolarization wave along the myofiber direction. Subendocardial wave velocities were prescribed higher than those in the rest of the myocardium to represent the influence of the Purkinje system (Figure 4).

The constant $k$ ($2{\cdot}1 \times 10^{-4}$ $m^2$ $s^{-1}$) determines the influence of wave-front curvature on wave velocity. The dimensionless tensor $\boldsymbol{M}$ describes anisotropy of wave propagation in the global coordinate system. It is related to the tensor $\boldsymbol{M}^*$, which in its turn is referred to a local coordinate system, aligned with the myofiber:

$$\boldsymbol{M} = \boldsymbol{R}\boldsymbol{M}^* \boldsymbol{R}^T. \tag{5}$$

The rotation tensor **R** is associated with the myofiber orientation; the index$^T$ indicates the transpose. The largest principal component along the myofiber direction is $m^*_{11} = 1$. The other principal components are $m^*_{22} = m^*_{33} = a^{-2}$, where $a$ is defined as the ratio of the velocity along the myofiber and that perpendicular to the myofiber (Figure 4).

With the assumption that the LV is electrically insulated, the wave fronts are perpendicular to the boundary $\Gamma_{ext}$, being the basal, endocardial, and epicardial surface of the cardiac wall:

$$\vec{n} \cdot \boldsymbol{M}\vec{\nabla} t_{dep} = 0 \quad \text{at} \quad \Gamma_{ext}. \tag{6}$$

The vector $\vec{n}$ is the unit vector normal to the boundary $\Gamma_{ext}$. Depolarization was started by prescribing essential boundary conditions $t_{dep} = 0$ at $\Gamma_{stim}$ (Figure 4):

$$t_{dep} = 0 \quad \text{at} \quad \Gamma_{stim}. \tag{7}$$

### 2.3. MECHANICS

The geometry, as obtained from the MR images, was defined as the reference state of zero transmural pressure in the simulations of cardiac mechanics.

Within the cardiac wall the equation of conservation of momentum was used while neglecting volumetric and inertial forces:

$$\vec{\nabla} \cdot \boldsymbol{\sigma} = \vec{0}. \tag{8}$$

The total Cauchy stress $\boldsymbol{\sigma}$ in the tissue was composed of a passive ($\boldsymbol{\sigma}_p$) and an active component ($\sigma_a$) along the myofiber direction $\vec{e}_f$:

$$\boldsymbol{\sigma} = \boldsymbol{\sigma}_P + \sigma_a \vec{e}_f \vec{e}_f. \tag{9}$$

Passive tissue stress $\boldsymbol{\sigma}_p$ was related to the deformation-gradient tensor $\boldsymbol{F}$ and the Green-Lagrange strain tensor $\boldsymbol{E}$ by:

$$\boldsymbol{\sigma}_p = \frac{1}{\det(\boldsymbol{F})} \boldsymbol{F} \cdot \frac{\partial W_p}{\partial \boldsymbol{E}} \cdot \boldsymbol{F}^T \quad \text{with } \boldsymbol{E} = \frac{1}{2}(\boldsymbol{F}^T \cdot \boldsymbol{F} - \boldsymbol{I}). \tag{10}$$

Symbol $\boldsymbol{I}$ represents the identity tensor. $W_p$ represents the deformation-energy density as a function of strain $\boldsymbol{E}$, being composed of an isotropic component $W_i$, related to tissue-shape change, a component $W_f$, related to the extra stiffness of the material in the myofiber direction, and a component $W_v$, related to volume change [19]

$$W_p = W_i + W_f + W_v \tag{11}$$

with

$$W_i = a_0 \cdot (\mathrm{e}^{\mathrm{a_1 I_1^2 + a_2 I_2}} - 1), \tag{12}$$

$$W_f = a_3 \cdot (\mathrm{e}^{\mathrm{a_4 E_f^2}} - 1), \tag{13}$$

$$W_v = a_5[\det(\boldsymbol{F}^T \cdot \boldsymbol{F}) - 1]^2, \tag{14}$$

where $I_1$ and $I_2$ represent the first and second invariants of $\boldsymbol{E}$, respectively [26, p. 89]. Material parameter values $a_0$ through $a_5$ are listed in Table 1.

$E_f$ represents the Green-Lagrange strain component along the myofiber direction:

$$E_f = \frac{1}{2}[(\frac{l_s}{l_{s0}})^2 - 1] \tag{15}$$

with actual sarcomere length $l_s$, and sarcomere length in the reference state $l_{s0} = 1{\cdot}9\ \mu$m.

The characteristics of active stress $\sigma_a$ were modeled using a contractile element, with length $l_c$, in series with an elastic element, with length $l_s - l_c$ [29]. The magnitude of $\sigma_a$ was described by

$$\sigma_a = f_1(t_a, l_s, l_c), \tag{16}$$

where $t_a$ represents time elapsed since depolarization. The time course of $l_c$ is described by a first-order differential equation:

$$\frac{\partial l_c}{\partial t} = f_2(l_s - l_c). \tag{17}$$

*Table 1.* Passive material tissue properties based on uni and bi-axial measurements of myocardial tissue slabs [27] and on the pressure-volume relationship of passive inflation of the LV [28].

| $a_0$ | $a_1$ | $a_2$ | $a_3$ | $a_4$ | $a_5$ |
|---|---|---|---|---|---|
| kPa | – | – | kPa | – | kPa |
| 0·5 | 3·0 | 6·0 | 0·01 | 60 | 55 |

The used functions $f_1$ and $f_2$ are described in the Appendix.

### 2.4. Boundary conditions

To prevent rigid-body motion, motion in the base-to-apex direction was set to zero at the base. In three points (anterior, posterior, and lateral) at the LV basal endocardium circumferential motion was also set to zero. Pressure loads on the LV and RV endocardium were assumed to be homogeneous, and equal to LV cavity pressure $p_{lv}$ and RV cavity pressure $p_{rv}$, respectively, while the load on the epicardium was assumed zero:

$$\vec{n} \cdot \boldsymbol{\sigma} \cdot \vec{n} = 0 \quad \text{at the epicardium,} \tag{18}$$

$$\vec{n} \cdot \boldsymbol{\sigma} \cdot \vec{n} = p_{lv} \quad \text{at the LV endocardium,} \tag{19}$$

$$\vec{n} \cdot \boldsymbol{\sigma} \cdot \vec{n} = p_{rv} \quad \text{at the RV endocardium.} \tag{20}$$

LV mitral and RV tricuspid inflows were simulated by prescribing a realistic pressure increase in the non-activated ventricles from 0 to 1 kPa in the LV and from 0 to 0·25 kPa in the RV. LV and RV pressures in the isovolumic contraction and relaxation phases were estimated [30] such that LV and RV cavity volumes remained constant within ±0·5%. During ejection, LV and RV pressures were related to aortic and pulmonary flow, respectively with three-element Windkessel models [31] (Figure 5).

The aortic and pulmonary Windkessel models were not coupled. For the LV and RV, a characteristic input impedance $Z_{a0}$ ($1{\cdot}2 \times 10^7$ and $0{\cdot}6 \times 10^7$ Pa·s·m$^3$, respectively) was put in series with a compliance $C_{\text{art}}$ ($1{\cdot}4 \times 10^{-9}$ and $5{\cdot}8 \times 10^{-9}$ m$^3$·Pa$^{-1}$) that was parallel to the peripheral flow resistance $R_{\text{per}}$ ($1{\cdot}2 \times 10^8$ and $1{\cdot}65 \times 10^7$ Pa·s·m$^{-3}$). The aortic and pulmonary valves opened when cavity pressures exceeded end-diastolic aortic and pulmonaric pressures, which were set at 10 and 2 kPa, respectively. Reversal of flows closed the valves.

### 2.5. Computational method

The equations were solved using the finite-element package SEPRAN (SEPRA, Leidschendam, the Netherlands) on a 64-bit Origin 200 computer (SGI, Mountain View, CA, USA), using a single processor at 225 MHz on a UNIX platform. The eikonal-diffusion equation was discretized with 8-noded Galerkin-type hexahedral elements having trilinear interpolation of the field of depolarization times. The ventricles were subdivided into 33536 elements with 37405 degrees of freedom with a mean spatial resolution 1·1 mm. The solution was facilitated by gradual increase of the nonlinear term in each successive Newton iteration [32, Chapter 1],

[33, p. 55]. A classical upwind scheme (Streamline Upwind Petrov Galerkin, [34]) was used to stabilize the finite-element calculations [35].

The equations related to mechanics were discretized with 27-noded hexahedral elements with triquadratic interpolation of the displacement field. The ventricles were subdivided into 224 elements, with 6723 degrees of freedom.

The calculation time for simulation of a complete cardiac cycle was approximately 30 hours.

### 2.6. Simulations and data analysis

Three simulations were performed. A normal cardiac cycle was simulated in which myofibers were activated synchronously (SYNC simulation) as described [19]. Furthermore, simulations of pacing at the RV apex (PACERV simulation) and LV free wall (PACELV simulation) were performed.

Global hemodynamics and myofiber natural strains $\epsilon_f$ were computed as a function of time [19]. Stroke-work density $W_f$[J · m$^{-3}$] was computed from $\epsilon_f$ and Cauchy myofiber stress $\sigma_f$ by

$$W_f = \oint_{\text{cardiac cycle}} \sigma_f \, \mathrm{d}\, \epsilon_f. \tag{21}$$

## 3. Results

### 3.1. Geometry

Fit orders $L$ (Equation (2)) for the epicardial, LV endocardial, and RV free wall and septal surface (Figure 2) were set to 6, 6, 5, and 5, respectively. For these surfaces, the root-mean-squared distance between the original and fitted position of the data points was 0·80 mm, 0·86 mm, 0·36 mm and 0·48 mm, respectively. LV cavity, LV wall (LV free wall and septum), and RV free-wall volumes were 26·2, 17·2, 57·6, and 7·90 ml, respectively (Figure 3).

### 3.2. Global behavior

Maximum ventricular pressures and ejection fractions in the SYNC simulation were slightly larger than in both simulations of pacing (Figure 6, Table 2). $\mathrm{d}p/\mathrm{d}t_{\max}$ for both the LV and RV was largest in the SYNC simulation as compared to the simulations of pacing, except for the LV in the PACELV simulation. When the LV was paced, left ventricular $\mathrm{d}p/\mathrm{d}t_{\max}$ was larger than left ventricular $\mathrm{d}p/\mathrm{d}t_{\max}$ when the RV was paced. Similarly, when the RV was paced, right ventricular $\mathrm{d}p/\mathrm{d}t_{\max}$ was larger then right ventricular $\mathrm{d}p/\mathrm{d}t_{\max}$ when the LV was paced.

In both the SYNC and PACERV simulations, $\mathrm{d}p/\mathrm{d}t_{\max}$ was reached earlier in the RV than for the LV. In the PACELV simulation, $\mathrm{d}p/\mathrm{d}t_{\max}$ was reached earlier in the LV. In all simulations, stroke volume was larger for the LV than the RV. In the SYNC and PACERV simulations, the RV entered the ejection phase 24 and 26 ms before the LV, respectively (Table 2). In the PACELV simulation, the LV entered this phase 12 ms before the RV. The ejection phase lasted longer for the LV than for the RV in all simulations.

*Table 2.* Hemodynamic variables in the SYNC, PACERV, and PACELV simulations; $p_{max}$ maximum cavity pressure; $dp/dt_{max}$ maximum first time derivative of cavity pressure; $q_{max}$ maximum outflow; $V_{be}$ and $V_{ee}$ cavity volume at beginning and end of the ejection phase; respectively; $V_w$ wall volume; $V_s$ stroke volume; *EF* ejection fraction; $t_{dp/dt_{max}}$ moment of $dp/dt_{max}$; $\Delta t_{ic}$ duration of isovolumic contraction phase; $t_{bej}$ beginning of ejection phase; $\Delta t_{ej}$ duration of ejection phase

| | | SYNC | | PACERV | | PACELV | |
|---|---|---|---|---|---|---|---|
| | | LV | RV | LV | RV | LV | RV |
| $p_{max}$ | kPa | 13·2 | 3·2 | 12·9 | 3·15 | 13·1 | 2·98 |
| $dp/dt_{max}$ | kPa/s | 206 | 84·9 | 137 | 73·5 | 240 | 55·1 |
| $q_{max}$ | ml/s | 221 | 207 | 199 | 190 | 213 | 159 |
| $V_{be}/V_w$ | – | 0·95 | 3·25 | 0·95 | 3·26 | 0·95 | 3·29 |
| $V_{ee}/V_w$ | – | 0·54 | 1·31 | 0·57 | 1·33 | 0·55 | 1·34 |
| $V_s$ | ml | 23·5 | 15·3 | 22·3 | 15·2 | 23·4 | 15·3 |
| EF | % | 42·9 | 59·7 | 40·5 | 59·1 | 42·5 | 59·1 |
| $t_{dp/dt_{max}}$ | ms | 234 | 230 | 282 | 280 | 300 | 314 |
| $\Delta t_{ic}$ | ms | 58 | 34 | 106 | 80 | 114 | 212 |
| $t_{bej}$ | ms | 258 | 234 | 306 | 280 | 314 | 126 |
| $\Delta t_{ej}$ | ms | 176 | 164 | 174 | 170 | 174 | 164 |

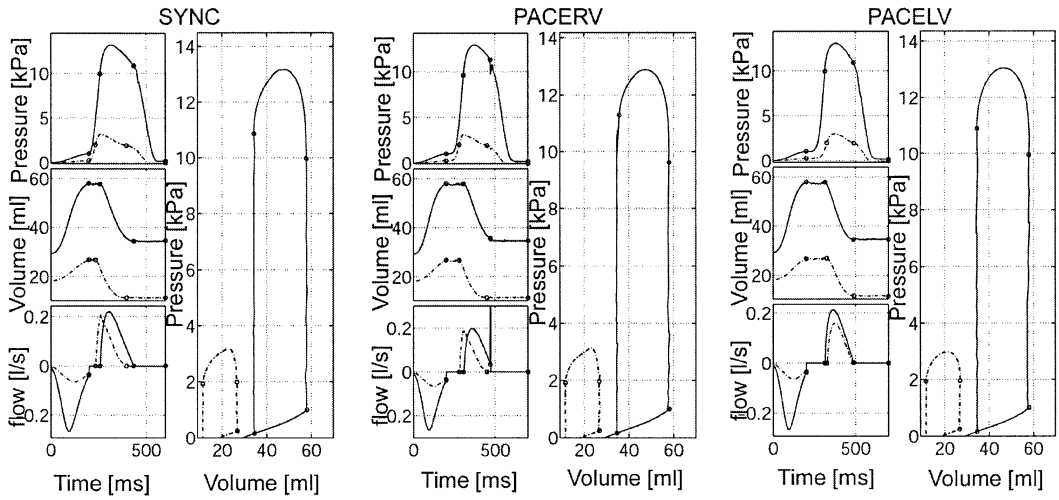


*Figure 6.* Global hemodynamics in the LV (–) and RV (- .) in the SYNC, PACERV, and PACELV simulations. The left panels for each simulation represent from top to bottom: cavity pressure [kPa]; cavity volume [ml] and flow [l/s] as a function of time. Mitral and tricuspid inflow were defined as negative and aortic and pulmonary outflow as positive. Dots indicate moments of opening and closure of the valves. The right panels for each simulation represent the pressure-volume loops.

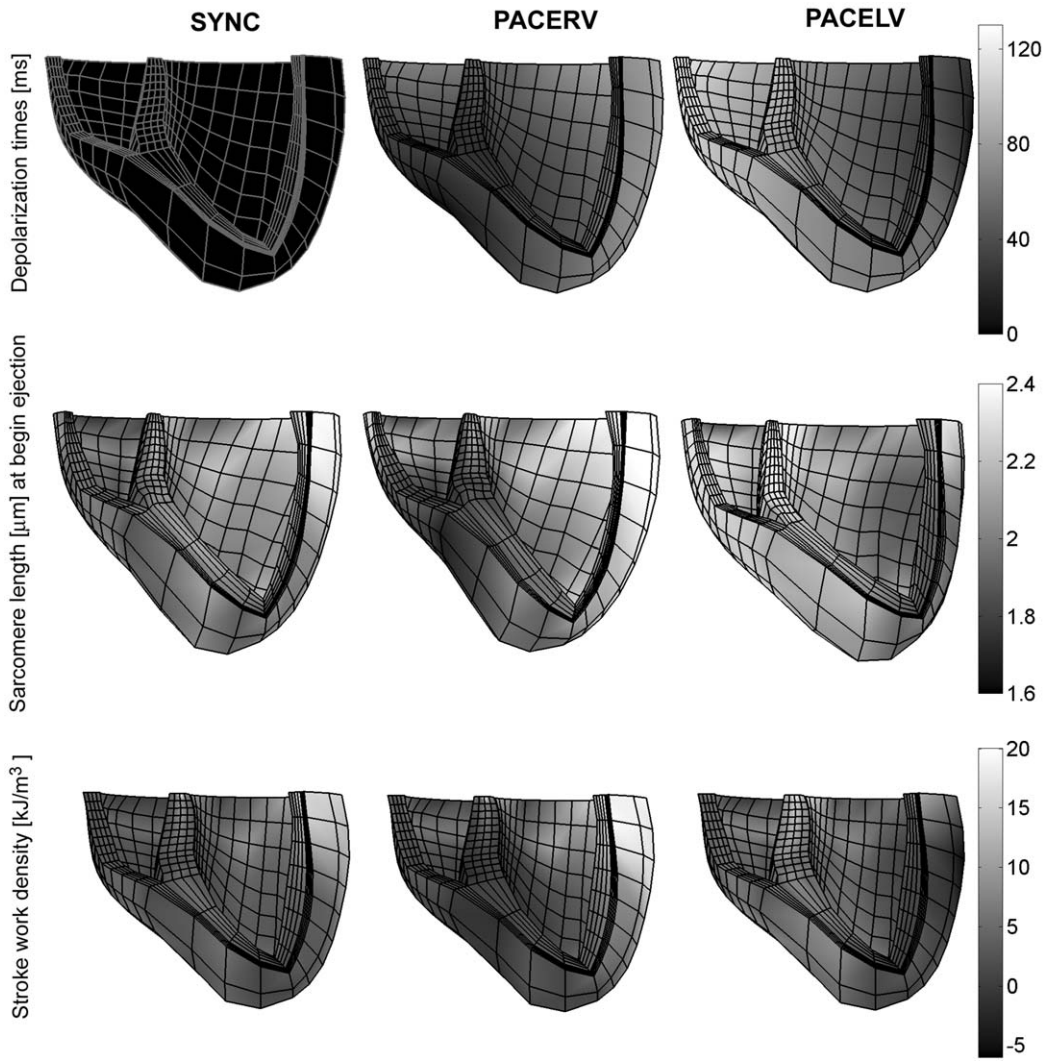


*Figure 7.* Anterior views of the heart, showing cross-sections of the walls, and LV and RV endocardium. Top panel: depolarization times [ms] for the SYNC, PACERV, and PACELV simulations, represented on the deformed mesh at end-diastole. Mid panel: sarcomere length [$\mu$m] for the latter mentioned simulations. Sarcomere length is represented on the deformed mesh at the beginning of LV ejection. Bottom panel: stroke work density [kJ·m$^{-3}$] for the simulations. The stroke work is represented on the undeformed mesh in the reference state.

### 3.3. Regional behavior

Depolarization times for the SYNC, PACERV, and PACELV simulations are shown in the top row of Figure 7. Depolarization for the SYNC simulation was completely synchronous, with depolarization times $t_{\text{dep}} = 0$ for all myofibers. Complete depolarization of the heart was faster in the PACERV (92 ms) than in the PACELV simulation (129 ms). In the PACERV and PACELV simulations, the waves ended at the base of the left and right ventricular free wall, respectively.

Sarcomere length [$\mu$m] at the beginning of LV ejection and stroke-work density [kJ·m$^{-3}$] are shown in the mid and bottom row of Figure 7, respectively. For the SYNC simulation,

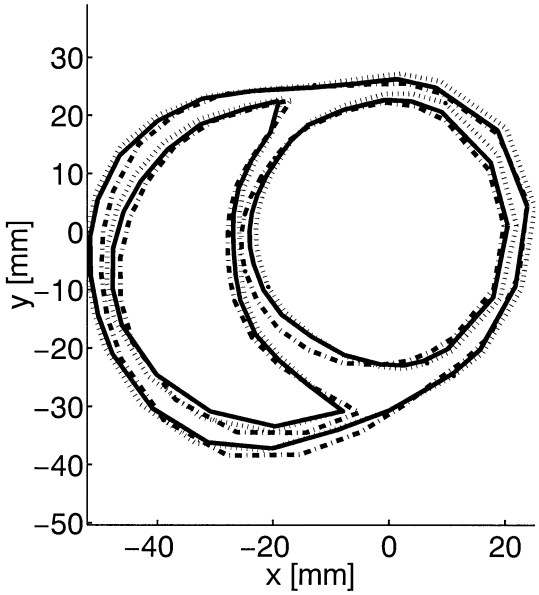


*Figure 8.* Basal contours of the epicardium and LV and RV endocardium at the beginning of LV ejection for the SYNC (−), PACERV (...), and PACELV (- .) simulations. Notice the movement of the septum to the LV and RV side relative to the SYNC simulation for RV apex pacing and pacing at the LV free wall, respectively.

sarcomere length was larger in the LV subendocardium than in the RV subendocardium. Sarcomere length and stroke work were distributed relatively homogeneously, except for a region in the LV base. Furthermore, in both simulations of pacing, sarcomere length and stroke work were dependent on the sequence of depolarization: low values were observed in the early depolarized regions, and high values in late ones. In the PACERV simulation, the septum and RV free wall thickened early, whereas the LV free wall was still relatively thin. The LV apex moved towards the RV side. In the PACELV simulation, the LV free wall thickened early, whereas the septum and RV free wall were still relatively thin. The LV apex moved away from the RV.

For a better view on septal motion, a short-axis view of the basal area has been depicted in Figure 8 for the beginning of LV ejection. Relative to the septum in the SYNC simulation, the septum in the PACERV moved towards the LV side. In the PACELV simulation, the septum moved towards the RV side.

## 4. Discussion and conclusions

We have presented a three-dimensional finite-element model of RV and LV electromechanics. With the model, complete cardiac cycles of a normal heart beat and pacing at the RVA and LVFW were simulated. Myofiber strain and stroke-work density were found to be determined by the sequence of depolarization. The earliest activated ventricle had the earliest start of ejection, while at the beginning of ejection the septum moved towards the last activated ventricle. The potential of the model for simulating conduction disturbances in a realistic cardiac geometry has been demonstrated: the geometry of the mesh was based on short axis MR images of a dog obtained non-invasively.

### 4.1. RESULTS

The depolarization sequence for LVFW pacing was in agreement with previously reported measurements [36]. In the simulations with ventricular pacing, during the isovolumic contraction phase, myofibers shortened rapidly in the early depolarized regions, whereas in the late depolarized regions, myofibers were pre-stretched, as has been reported previously [37, 38]. The pattern of stroke-work density was also similar to experimentally determined patterns [7].

In both simulations of pacing, maximum pressure and $dp/dt_{max}$ (except for $dp/dt_{max,LV}$ for LV pacing) decreased as compared to normal sinus rhythm, as has also been reported earlier [39].

Considering interventricular asynchrony, the following agreement with experiments has also been observed. In the SYNC simulation the RV entered the ejection phase before the LV, as was also reported previously for the canine heart [3]. In simulating pacing of the LV, this ventricle entered the ejection phase first [3], while the septum moved towards the RV. In simulating pacing of the RV, the opposite was observed: the RV entered the ejection phase before the LV. A behavior as found in the simulations has also been reported in measurements on patients with a left bundle branch block (LBBB), where the depolarization sequence is similar to RV apex pacing [6]. The septum flattened and moved towards the LV [6, 2]. Therefore, good qualitative and quantitative agreement has been found between model and experiment, not only for regional mechanical behavior, but also for the timing and degree of pressure development and timing of volume ejection, as well as septal displacement.

### 4.2. LIMITATIONS

The simulations were performed to demonstrate the potential for patient-specific modeling of cardiac electromechanics during ventricular pacing. Due to simplifications, some non-physiological behavior is still observed.

The reference geometry corresponds to the end-diastolic state of a canine heart. Since the depolarization wave propagates mainly during this phase, the latter geometry is suitable for solving timing of depolarization. However, for solving mechanics, this state does not correspond to the unloaded reference state. In the model, the cavity-to-wall volume ratios in the reference state was 0·51. In the real LV, cavity-to-wall volume ratio in the state of zero cavity pressure is about 0·30 [40].

We assumed mechanical and electrical properties to be the same in the ventricles. However, the RV and LV are somewhat different regarding the electromechanical properties [41].

Myofiber orientation was assumed to vary linearly from endocardium to epicardium. Previously [30, 14, 42], it has been shown that spatial distribution of local wall mechanics is very sensitive to the choice of the myofiber orientation. We attribute the inhomogeneity of stroke work (Figure 7) to a suboptimal choice of the myofiber orientation.

Filling and stroke volume were not similar for both ventricles. For one heart beat it is possible that one ventricle ejects slightly more blood than the other. However, on average, filling and ejection have to be equal for the LV and RV. We attribute the difference in stroke volume to the settings of end-diastolic filling pressure and aortic/pulmonary pressure at the beginning of ejection, because the two Windkessel models, for the aortic and pulmonary arteries, were uncoupled. Also, pressures and volumes at the end of the cycle were not equal to pressure and volumes at the beginning of the cycle, *i.e.*, the solution was not periodic. Equal LV and RV ejection and periodicity will be obtained by embedding the heart model in a lumped-parameter model of the complete circulation.

In conclusion, a three-dimensional finite-element model of electromechanics in the left and right ventricles has been developed. During sinus rhythm ventricular ejection started earlier for the right side than for the left side.

In simulations with ventricular pacing, results agreed with experimental findings in the following aspects: 1) depolarization sequence; 2) the spatial distributions of sarcomere length and stroke-work density depended mainly on timing of depolarization; 3) maximum pressure and maximum increase of pressure were lower than during sinus rhythm; 4) the earliest activated ventricle had the earliest start of ejection, and 5) the septum moved towards the last activated ventricle at the onset of systole.

As a first step, the potential of patient-specific modeling in simulating conduction disturbances has been demonstrated by inserting a ventricular geometry (rms error 0·8 mm), obtained from non-invasively measured short axis MR images of a dog. Next steps would include the implementation of adaptation models to estimate patient myofiber orientation and to assess the effects of pacing in the long term.

**Acknowledgements**

The study has been financially supported by Medtronic Bakken Research Center Maastricht. Thanks goes to Ryan Lahm at Medtronic, Minneapolis, MN for providing the MR data set.

**Appendix A, model of active stress development**

Active stress was dependent on sarcomere length $l_s$, length $l_c$ of the contractile element, and time $t_a$, elapsed since the moment of electrical depolarization:

$$\sigma_a = f_1(t_a, l_s, l_c) = \frac{l_s}{l_{s0}} f_{\text{iso}}(l_c) f_{\text{twitch}}(t_a, l_s)(l_s - l_c)E_a, \tag{A1}$$

where $l_{s0}$ represents the sarcomere length in the reference state, and $E_a$ is the stiffness of the serial elastic element.

The dependency of isometrically developed active stress on $l_c$ was represented by

$$f_{\text{iso}}(l_c) = \begin{cases} 0 & l_c \le a_7 \\ T_0 \cdot \tanh^2(a_6(l_c - a_7)) & l_c > a_7 \end{cases}, \tag{A2}$$

which is similar to measurements reported in [43] on rat cardiac trabecula at an intracellular calcium concentration of approximately 7 $\mu$M.

The dependency of myofiber stress on $t_a$ and $l_s$ was represented by

$$f_{\text{twitch}}(t_a, l_s) = \begin{cases} 0 & t_a < 0 \\ \tanh^2(\frac{t_a}{t_r}) \tanh^2(\frac{t_{\max} - t_a}{t_d}) & 0 \le t_a \le t_{\max} \\ 0 & t_a > t_{\max} \end{cases}, \tag{A3}$$

with

$$t_{\max} = b(l_s - l_d), \tag{A4}$$

where $t_r$ is the activation rise time constant, $t_d$ the activation decay time constant, and $t_{\max}$ the activation duration. Parameter $b$ relates activation duration to the length of a sarcomere $l_s$. $l_d$ is the sarcomere length for which this duration is 0.

*Table 3.* Active material properties used

| $a_6$ | $a_7$ | $T_0$ | $E_a$ | $v_0$ | $l_{s0}$ | $t_r$ | $t_d$ | b | $l_d$ |
|---|---|---|---|---|---|---|---|---|---|
| $\mu m^{-1}$ | $\mu m$ | kPa | $\mu m^{-1}$ | $\mu m \cdot s^{-1}$ | $\mu m$ | s | s | $s \cdot \mu m^{-1}$ | $\mu m$ |
| 2·0 | 1·5 | 180 | 20 | 7·5 | 1·9 | 0·075 | 0·075 | 0·15 | −0·4 |

The time course of the contractile element length $l_c$ was simulated by a first-order differential equation (function $f_2$ in Equation (17)):

$$\frac{\partial l_c}{\partial t} = (E_a(l_s - l_c) - 1)v_0, \tag{A5}$$

where $v_0$ represents the unloaded shortening velocity. The values of the parameters are listed in Table 3. Equation (26) was solved using an Adams-Bashfort-Moulton multi-step integration scheme [44, pp. 952–954].

## References


1. D. Durrer, R. T. van Dam, G. E. Freud, M. J. Janse, F. L. Meijler and R. C. Arzbaecher, Total excitation of the isolated human heart. *Circulation* 41 (1970) 899–912.
2. W. C. Little, R. C. Reeves, J. Arciniegas, R. E. Katholi and E. W. Rogers, Mechanisms of abnormal interventricular septal motion during delayed left ventricular activation. *Circulation* 65 (1982) 1486–1491.
3. X. A. A. M. Verbeek, K. Vernooy, M. Peschar, T. van der Nagel, A. van Hunnik and F. W. Prinzen, Quantification of interventricular asynchrony during lbbb and ventricular pacing. *Amer. J. Physiology* 283 (2002) H1370–H1378.
4. F. W. Prinzen, C. H. Augustijn, T. Arts, M. A. Allessie and R. S. Reneman, Redistribution of myocardial fiber strain and blood flow by asynchronous activation. *Amer. J. Physiol.* 259 (1990) H300–H308.
5. L. K. Waldman and J. W. Covell, Effects of ventricular pacing on finite deformation in canine left ventricles. *Amer. J. Physiol.* 252 (1987) H1023–H1030.
6. C. L. Grines, T. M. Bashore, H. Boudoulas, S. Olson, P. Shafer and C. F. Wooley, Functional abnormalities in isolated left bundle branch block. *Circulation* 79 (1989) 845–853.
7. F. W. Prinzen, W. C. Hunter, B. T. Wyman and E. R. McVeigh, Mapping of regional myocardial strain and work during ventricular pacing: experimental study using magnetic resonance imaging tagging. *J. Amer. Coll. Cardiol.* 33 (1999) 1735–1742.
8. F. W. Prinzen, C. H. Augustijn, M. A. Allessie, T. Arts, T. Delhaas and R. S. Reneman, The time sequence of electrical and mechanical activation during spontaneous beating and ectopic stimulation. *Eur. Heart J.* 13 (1992) 535–543.
9. M. F. M. Oosterhout van, F. W. Prinzen, T. Arts, J. J. Schreuder, W. Y. R. Vanagt, J. P. M. Cleutjens and R. S. Reneman, Asynchronous electrical activation induces inhomogenous hypertrophy of the left ventricular wall. *Circulation* 98 (1998) 588–595.
10. H. R. Andersen, J. C. Nielsen and P. E. B. Thomsen, Long-term follow-up of patients from a randomised trial of atrial versus ventricular pacing for sick-sinus syndrome. *Lancet* 350 (1997) 1210–1216.
11. B. L. Wilkoff, J. R. Cook and A. E. Epstein, Dual-chamber pacing or ventricular back-up pacing in patients with an implantable defibrillator. *J. Amer. Med. Assoc.* 288 (2002) 3115–3123.
12. F. W. Prinzen and M. Peschar, Relation between the pacing induced sequence of activation and left ventricular pump function in animals. *J. Pacing Clin. Electrophysiol.* 25 (2002) 484–498.
13. P. H. M. Bovendeerd, J. M. Huyghe, T. Arts, D. H. van Campen and R. S. Reneman, Influence of endocardial-epicardial crossover of muscle fibers on left ventricular wall mechanics. *J. Biomech.* 27 (1994) 941–951.
14. J. Rijcken, P. H. M. Bovendeerd, A. J. G. Schoofs, D. H. van Campen and T. Arts, Optimization of cardiac fiber orientation for homogeneous fiber strain during ejection. *An. Biomed. Eng.* 27 (1999) 289–297.

15. T. P. Usyk, J. H. Omens and A. D. McCulloch, Regional septal dysfunction in a three-dimensional computational model of focal myofiber disarray. *Amer. J. Physiol.* 281 (2001) H506–H514.
16. P. H. M. Bovendeerd, T. Arts, T. Delhaas, J. M. Huyghe, D. H. van Campen and R. S. Reneman, Regional wall mechanics in the ischemic left ventricle: numerical modeling and dog experiments. *Amer. J. Physiol.* (1996) H398–H409.
17. T. Mazhari, J. H. Omens, J. W. Covell and A. D. McCulloch, Structural basis of regional dysfunction in acutely ischemic myocardium. *Cardiovascular Res.* 47 (2000) 284–293.
18. L. A. Taber and W. W. Podszus, A laminated shell model for the infarcted left ventricle. *Int. J. Solids Struct.* 34 (1997) 223–241.
19. R. C. P. Kerckhoffs, P. H. M. Bovendeerd, J. C. S. Kotte, F. W. Prinzen, K. Smits and T. Arts, Homogeneity of cardiac contraction despite physiological asynchrony of depolarization: A model study. *Ann. Biomed. Eng.* 31 (2003) 536–547.
20. T. P. Usyk, I. J. LeGrice and A. D. McCulloch, Computational model of three-dimensional cardiac electromechanics. *Comput. Visual. Sci.* 4 (2002) 249–257.
21. D. D. Streeter, Gross morphology and fiber geometry of the heart. In: R. M. Berne (ed.), *Handbook of Physiology – The Cardiovascular System I. Am. Physiol. Soc.* (1979) pp. 61–112.
22. R. C. P. Kerckhoffs, O. P. Faris, P. H. M. Bovendeerd, F. W. Prinzen, K. Smits, E. R. McVeigh and T. Arts, Timing of depolarization and contraction in the paced canine left ventricle: model and experiment. Accepted for *J. Cardiovasc. Electrophysiol.* (2003).
23. W. G. O'Dell and A. D. McCulloch, Imaging three-dimensional cardiac function. *Annu. Revisions Biomed. Eng.* 2 (2000) 431–456.
24. W. G. O'Dell, C. C. Moore, W. C. Hunter, E. A. Zerhouni and E. R. McVeigh, Three-dimensional myocardial deformations: calculation with displacement field fitting to tagged mr images. *Radiology* 195 (1995) 829–835.
25. P. Colli-Franzone, L. Guerri and S. Tentoni, Mathematical modeling of the excitation process in myocardial tissue: influence of fiber rotation on wavefront propagation and potential field. *Math. Biosci.* 101 (1990) 155–235.
26. L. E. Malvern, *Introduction to the Mechanics of a Continuous Medium.* Englewood Cliffs, NJ: Prentice Hall, Inc. (1969) 713 pp.
27. V. P. Novak, F. C. P. Yin and J. D. Humphrey, Regional mechanical properties of passive myocardium. *J. Biomech.* 27 (1994) 403–412.
28. S. Nikolić, E. L. Yellin, K. T. Tamura, H. Vetter, T. Tamura, J. S. Meisner, and R. W. M. Frater, Passive properties of canine left ventricle: diastolic stiffness and restoring forces. *Circulation Res.* 62 (1988) 1210–1222.
29. T. Arts, P. C. Veenstra and R. S. Reneman, Epicardial deformation and left ventricular wall mechanics during ejection in the dog. *Am. J. Physiol.* 243 (1982) H379–H390.
30. P. H. M. Bovendeerd, T. Arts, D. H. van Campen and R. S. Reneman, Dependence of local left ventricular wall mechanics on myocardial fiber orientation: a model study. *J. Biomech.* 25 (1992) 1129–1140.
31. N. Westerhof, G. Elzinga and G. C. van den Bos, Influence of central and peripherical changes on the hydraulic input impedance of the systemic arterial tree. *Med. Biol. Engng.* 11 (1973) 710–723.
32. E. L. Allgower and K. Georg, *Numerical Continuation Methods: an Introduction.* Berlin: Springer-Verlag (1990) 388 pp.
33. K. A. Tomlinson, *Finite Element Solution of an Eikonal Equation for Excitation Wavefront Propagation in Ventricular Myocardium.* Ph.D. thesis, The University of Auckland (2000) 196 pp.
34. A. N. Brooks and T. J. R. Hughes, Stream-line upwind/Petrov-Galerkin formulation for convection dominated flows with particular emphasis on the incompressible Navier-Stokes equations. *Comp. Methods Appl. Mech. Engng.* 32 (1982) 199–259.
35. P. Colli-Franzone, L. Guerri, M. Pennacchio and B. Taccardi, Spreading of excitation in 3-d models of the anisotropic cardiac tissue. ii. effects of fiber architecture and ventricular geometry. *Math. Biosciences* 113 (1998) 145–209.
36. M. S. Spach and R. C. Barr, Analysis of ventricular activation and repolarization from intramural and epicardial potential distributions for ectopic beats in the intact dog. *Circulation Res.* 37 (1975) 830–843.
37. O. P. Faris, F. J. Evans: D. B. Ennis, P. A. Helm, J. L. Taylor, A. S. Chesnick, M. A. Guttman, C. Ozturk and E. R. McVeigh, Novel technique for cardiac electromechanical mapping with mri tagging and an epicardial electrode sock. *Ann. Biomedical Engng.* 31 (2003) 430–440.

38. B. T. Wyman, W. C. Hunter, F. W. Prinzen and E. R. McVeigh, Mapping propagation of mechanical activation in the paced heart with mri tagging. *Amer. J. Physiology* 276 (1999) H881–H891.
39. M. Peschar, H. de Swart, K. J. Michels, R. S. Reneman and F. W. Prinzen, Left ventricular septal and apex pacing for optimal pump function in canine hearts. *J. Amer. Coll. Cardiology* 41 (2003) 1218–1226.
40. T. Delhaas, T. Arts, P. H. M. Bovendeerd, F. W. Prinzen and R. S. Reneman, Subepicardial fiber strain and stress as related to left ventricular pressure and volume. *Am. J. Physiology* 264 (1993) H1548-H1559.
41. J. M. Capasso, E. Puntillo, G. Olivetti and P. Anversa, Differences in load dependence of relaxation between the left and right ventricular myocardium as a function of age in rats. *Circulation Res.* 68 (1989) 1499–1507.
42. M. Vendelin, P. H. M. Bovendeerd, J. Engelbrecht and T. Arts, Optimizing ventricular fibers: uniform strain or stress, but not ATP consumption, leads to high efficiency. *Amer. J. Physiology* 283 (2002) H1072–H1081.
43. H. E. D. J. ter Keurs, J. J. J. Bucx, P. P. de Tombe, P. Backx and T. Iwazumi, The effects of sarcomere length and Ca++ on force and velocity of shortening in cardiac muscle. In: H. Suga and G. H. Pollack (eds.), *Molecular Mechanisms of Muscle Contraction.* New York: Plenum (1988) pp. 581–593.
44. E. Kreyszig, *Advanced Engineering Mathematics*. ($8^{th}$ edition) New York: John Wiley (1999).
45. D. T. Lindsay, *Functional Human Anatomy.* St. Louis, Missouri: Mosby-Year Book, Inc (1996) 976 pp.